
Article:
Rusmin, R., Sarkar, B. orcid.org/0000-0002-4196-1225, Tsuzuki, T. et al. (2 more authors) (2017) Removal of lead from aqueous solution using superparamagnetic palygorskite nanocomposite: Material characterization and regeneration studies. Chemosphere, 186. pp. 1006-1015. ISSN 0045-6535

https://doi.org/10.1016/j.chemosphere.2017.08.036

Removal of lead from aqueous solution using superparamagnetic palygorskite nanocomposite: material characterization and regeneration studies

Ruhaida Rusmin[a,b*], Binoy Sarkar[a§*],Takuya Tsuzuki[c], Nobuyuki Kawashima[a], Ravi Naidu[d,e*]

[a] Future Industries Institute, University of South Australia, Building X, Mawson Lakes, SA 5095, Australia.

[b] Faculty of Applied Sciences, Universiti Teknologi MARA, 40450, Shah Alam, Selangor, Malaysia.

[c] Research School of Engineering, College of Engineering and Computer Science, Australian National University, Acton, ACT 2601, Australia.

[d] Global Centre for Environmental Remediation (GCER), The University of Newcastle, ATC Building, Callaghan, NSW 2308, Australia.

[e] CRC CARE – Cooperative Research Centre for Contamination Assessment and Remediation of the Environment, P.O. Box 486, Salisbury, SA 5106, Australia.

[§] Current address: Department of Animal and Plant Sciences, The University of Sheffield, Western Bank, Sheffield, S10 2TN, UK.

_____

[*]Corresponding authors:

E-mail: Binoy.Sarkar@unisa.edu.au (Binoy Sarkar)

E-mail: Ravi.Naidu@newcastle.edu.au (Ravi Naidu)

E-mail: ruhaida.rusmin@mymail.unisa.edu.au (Ruhaida Rusmin)

Graphical abstract

Highlights

- Superparamagnetic palygorskite nanocomposite was synthesized and characterized
- The nanocomposite adsorbed up to 63% more Pb^{2+} than palygorskite
- Easy magnetic separation of spent adsorbent was achieved within 60 to 120 sec
- EDTA performed the best to regenerate the spent adsorbent
- Magnetic susceptibility after 3 cycles of use reduced only slightly

Abstract

A palygorskite-iron oxide nanocomposite (Pal-IO) was synthesized in situ by embedding magnetite into the palygorskite structure through co-precipitation method. The physico-chemical characteristics of Pal-IO and their pristine components were examined through various spectroscopic and micro-analytical techniques. Batch adsorption experiments were conducted to evaluate the performance of Pal-IO in removing Pb(II) from aqueous solution. The surface morphology, magnetic recyclability and adsorption efficiency of regenerated Pal-IO using desorbing agents HCl (Pal-IO-HCl) and ethylenediaminetetraacetic acid disodium salt (EDTA-Na_2) (Pal-IO-EDTA) were compared. The nanocomposite showed a superparamagnetic property (magnetic susceptibility: 20.2 emu g^{-1}) with higher specific surface area (99.8 $m^2 g^{-1}$) than the pristine palygorskite (49.4 $m^2 g^{-1}$) and iron oxide (72.6 $m^2 g^{-1}$). Pal-IO showed a maximum Pb(II) adsorption capacity of 26.6 mg g^{-1} (experimental condition: 5 g L^{-1} adsorbent loading, 150 agitations min^{-1}, initial Pb(II) concentration from 10 to 500 mg L^{-1}, at 25°C) with easy separation of the spent adsorbent. The adsorption data best fitted to the Langmuir isotherm model (R^2=0.9995) and pseudo-second order kinetic model (R^2=0.9945). Pb(II) desorption using EDTA as the complexing agent produced no disaggregation of Pal-IO crystal bundles. and was able to preserve the composite's magnetic recyclability. Pal-IO-EDTA exhibited almost 64% removal capacity after three cycles of regeneration and preserved the nanocomposite's structural integrity and magnetic properties (15.6 emu g^{-1}). The nanocomposite holds advantages as a sustainable material (easily separable and recyclable) for potential application in purifying heavy metal contaminated wastewaters.

Key words: Palygorskite-iron oxide nanocomposite; Magnetic separation; Lead contamination; Desorption; Regeneration

1. Introduction

The heavy metal lead (Pb) ranks second in the Substance Priority List compiled by the Agency for Toxic Substances and Disease Registry (ATSDR) (ATSDR, 2015), which indicates the serious health and the environmental risk of this metal. Anthropogenically Pb(II) can occur in water sources through leaching and improper discharge from aging plumbing infrastructure, smelting activities, e-waste recycling and mining industries (Harvey et al., 2015; Yoshida et al., 2016). The Pb(II) contamination of water and soil remains a challenge primarily for less-developed countries due to the ineffective infrastructure, less stringent regulation and high costs associated with its remediation (Naidu, 2013; Yoshida et al., 2016).

Recently, engineered magnetic iron-based adsorbents for removing heavy metals from water received special interests due to their high specific surface area, less toxicity than other magnetic nanoparticles, and superparamagnetic properties (Ambashta and Sillanpää, 2010; Brigante et al., 2016; Su, 2017). Despite their efficiency and promising application in adsorbent separation, the key challenges for these iron-based materials lie on ensuring a cost-effective preparation method, addressing the aggregation issues and understanding their environmental fate (Xu et al., 2012; Su, 2017). To reduce the cost of synthesis and provide an environmentally friendly approach, magnetic adsorbents prepared from natural resources like biochar (Han et al., 2016), starch (Xiang et al., 2016) and clay minerals (Tian et al., 2016) were reported. However, the functionalization of magnetic composites with clay minerals is important to cater the challenges even better due to clays' easy availability, stability, low toxicity, and high affinity towards various water contaminants, such as pesticides, phenolic compounds, industrial dyes and heavy metals (Murray, 2006; Sarkar et al., 2012). In water treatment processes, magnetic-clay composites could also increase their contaminant adsorption efficiencies, and address issues related to spent adsorbent separation, which is

often encountered while using unmodified clays (Chen et al., 2016b). A huge focus was given previously towards the structural modification of magnetic clay nanocomposites for enhancing their adsorption efficacy (Pan et al., 2011; Tian et al., 2016). However, an assessment on the magnetic recyclability of the composites was rather inadequate. The fate and stability of magnetic particles in enduring the adsorption-desorption and recycling process has been scarcely studied. It is still unclear how the magnetic adsorbents evolve during the regeneration process and whether one can use those spent materials (after multiple cycles of reactions) for further removal of contaminants. The saturation magnetization (M_s) and magnetic coercivity (H_c) are important parameters for the environmental remediation application of magnetic adsorbents. The M_s and H_c, respectively, represent the magnetic strength and the ability of a magnetic material to resist de-magnetization. While a high M_s value indicates a strong magnetic interaction, a low magnetic coercivity means the material would be readily separated (precipitated) from the suspension upon exposure to an external magnetic field. The separated material can then be re-dispersed as a colloidal suspension once the external magnetic field is removed. Superparamagnetic materials have a negligible remanence and coercivity value that allow a rapid response to the applied external magnetic field. This is desirable for an efficient magnetic separation of spent adsorbent (Mahdavian and Mirrahimi, 2010).

In addition, understanding the clay's role in preserving the magnetic sustainability of the composite requires careful attention for endowing the material's practical application in water treatment. Therefore, this research attempts to understand the clay-iron oxide structural integration and how they cooperatively contribute in the Pb(II) adsorption and regeneration studies. The influence of desorbing agent and magnetic recyclability were studied through the measurement of magnetic properties, structural morphology and analytical approaches. The broader aim of this research is to develop a magnetic clay composite as a tool for remediating

heavy metals from contaminated wastewaters. Palygorskite, an abundant clay mineral in Australia, was used in this study instead of more commonly used smectite. Natural palygorskite is inexpensive (costs approximately US$0.20 kg^{-1}), has elongated chain or lath-like particles, and contains high specific surface area suitable for the preparation of adsorbents and barrier materials (Murray, 2006).

2. Materials and methods

2.1 Materials and reagents

Palygorskite originating in Western Australia was purchased from Hudson Resource Pty. Ltd., Australia, lead (II) nitrate ($Pb(NO_3)_2$) and ammonium hydroxide (NH_4OH, 25% v/v) from Fisher Scientific (United Kingdom), iron (III) chloride hexahydrate ($FeCl_3.6H_2O$) from Chem-Supply (Australia), iron (II) chloride tetrahydrate ($FeCl_2.4H_2O$) from Sigma-Aldrich (Germany), and ethylenediaminetetraacetic acid disodium salt (EDTA- Na_2) from Sigma-Aldrich (United States). All other reagents were of analytical or laboratory grade.

2.2 Preparation of palygorskite-iron oxide (Pal-IO) nanocomposite

A co-precipitation method (Pan et al., 2011) with some modifications was used to prepare the palygorskite-iron oxide nanocomposite (Pal-IO). An initial mass ratio of 2:1 of palygorskite:iron oxide was chosen. $FeCl_3.6H_2O$ (4.72 g) was dissolved in 180 mL Milli-Q water (resistivity ≥ 18 MΩ.cm) followed by the addition of 4.2 g palygorskite (Pal) into the solution. The Pal-Fe^{3+} aqueous suspension was ultra-sonicated for 30 min and transferred to a 3-necked bottle with continuous mixing for 3 h at 25°C. Then $FeCl_2.4H_2O$ (1.72 g) was added into the above suspension under continuous N_2 flow (50 mL min^{-1}). The temperature was increased to 80°C and then 10 mL of NH_4OH (25% v/v) was added drop-wise to the Pal-Fe^{3+}-Fe^{2+} suspension with vigorous stirring for 30 min. The black precipitate product (Pal-IO)

was separated via centrifugation and washed thoroughly with Milli-Q water and ethanol until the pH of the supernatant became neutral (~pH 7). The Pal-IO precipitate was dried at 110°C for 3 h, grinded with pestle and mortar, and sieved to obtain particle size <90 μm. For comparison purpose, iron oxide (IO) was also synthesized using the same procedure without the addition of palygorskite.

2.3 Material characterization

The surface morphology was examined by using a FEI Quanta 450 FEG Environmental Scanning Electron Microscope (SEM) at High Vacuum (HV) mode using an Everhart-Thornley detector. The sample was carbon coated (30 nm) using a QUORUM Q150T E Carbon Coater. The Transmission Electron Microscope (TEM) images were collected using a JEOL JEM-2100F-HR transmission electron microscope with accelerating voltage of 200 kV. The powder X-ray Diffraction (XRD) patterns were collected on a PANalytical Empyrean X-ray diffractometer using CuK_{α} radiation (λ = 1.5406 Å) operating at 40 mA and 40 kV with a step size of 0.0130. The patterns were recorded from 9 to 99° 2θ by using a 0.25° fixed divergence slit and 0.50° anti-scatter slit. For the Fourier Transform Infra-Red (FTIR) analysis, a 1:200 (w/w) ratio of sample: KBr was used for the pallet preparation. The spectra were collected using an Agilent Cary 600 series spectrometer (Agilent Technologies) in the range of 4000–400 cm^{-1} by the co-addition of 16 scans with a resolution of 8 cm^{-1}.The specific surface area (SSA) and pore size distribution were determined by BET (Brunauer–Emmett–Teller) and BJH (Barrett-Joyner-Halenda) methods, respectively, through N_2 gas adsorption-desorption experiments on a Micromeritics Gemini 2380 Surface Area Analyzer. The zeta potential values of the adsorbents in aqueous suspension (0.01% m/v) were measured on a zeta potential analyzer (Nicomp^{TM} 380 ZLS, USA). The thermo gravimetric analysis (TGA) was conducted on a Mettler Toledo Thermogravimetric Analyzer (TGA/DSC

160 1 model) equipped with STAR^{e} system with heating rate of 10°C min^{-1} from 25 to 950°C
161 under N_2 environment (50 mL min^{-1}). Magnetic measurement was conducted using a
162 Vibrating Sample Magnetometer (VSM) supplied by Princeton Measurement Corporation
163 (MicroMag^{TM} Model 3900 Series). The measurement was conducted in triplicates at 27°C
164 with applied field of 1 Tesla and averaging time of 100 to 200 ms.
165
166 2.4 Adsorption experiments
167 Aqueous solutions of Pb(II) with required concentrations (10, 20, 50, 100, 200, 300 and 500
168 mg L^{-1}) were prepared by dissolving $Pb(NO_3)_2$ in Milli-Q water followed by subsequent
169 dilutions. These concentrations were within the typical Pb concentration ranges found in
170 contaminated acid mine drainage water (Lottermoser, 2010). Batch adsorption experiments of
171 palygorskite-iron oxide nanocomposite (Pal-IO), pristine palygorskite (Pal) and iron oxide
172 (IO) were conducted (experimental condition: 25°C, pH 5, 5 g L^{-1} adsorbent loading, 150
173 agitations per min, contact time of 12 h) in capped polypropylene tubes at a pre-determined
174 Pb(II) concentration. The kinetic adsorption experiments were conducted under similar
175 conditions, with 1 mL aliquot being taken out from the suspension at pre-determined time
176 intervals for Pb(II) concentration measurement.
177 After each completed adsorption reaction, the supernatant of Pal-IO and IO were retrieved by
178 the magnetic separation process (using a bar magnet) followed by filtration through a 0.45
179 μm membrane filter. For palygorskite, the suspension was centrifuged at the relative
180 centrifugal force (RCF) of 1512 x g for 10 min before the membrane filtration. The initial and
181 equilibrium concentrations were determined using an Inductively Coupled Plasma Optical
182 Emission Spectrometer (ICP-OES) (Perkin Elmer, Optima 5300V) in duplicates and the mean
183 value was reported. Adsorption of Pb(II) on the walls of the polypropylene tube was
184 negligible.

185 The amount of Pb(II) adsorbed onto the adsorbent was calculated using Eq. 1:

186 $$q_e = \frac{(C_i - C_e)\,V}{m} \quad \text{.....Eq. 1}$$

187 where, q_e is the amount of metal adsorbed at equilibrium (mg g^{-1}), C_i and C_e are the initial
188 and equilibrium metal concentrations (mg L^{-1}), respectively, V is the volume (L) of the
189 solution, and m is the mass (g) of the adsorbent.

190

191 2.5 Adsorbent regeneration studies

192 The Pb(II)-loaded adsorbent obtained from the adsorption experiment with 100 mg L^{-1} Pb(II)
193 was first separated from the supernatant. The spent adsorbent was then dispersed (5 g L^{-1}
194 loading rate) into either EDTA-Na_2 or HCl solutions (both 0.01 M) and agitated (150
195 agitations per min) for 30 min on a reciprocating shaker. Afterwards the adsorbent was
196 thoroughly washed (3 times) with Milli-Q water until the pH of the wash-out water reached
197 the range of 6.0–6.5 and no Pb(II) was detected in the wash-out solution as determined by
198 ICP-OES. Then, the adsorbent was re-used for the subsequent adsorption cycle as described
199 previously (Section 2.4). The desorption percentage was calculated by using Eq. 2:

200 $$\text{Desorption}\ (\%) = \frac{\text{Amount of Pb desorbed}}{\text{Amount of Pb adsorbed}} \times 100 \quad \text{.....Eq. 2}$$

201

202 **3. Results and discussion**

203 3.1 Characterization of Pal-IO nanocomposite

204 The morphology of bare iron oxide (IO) particles was almost spherical, homogenous and
205 fairly well dispersed (Fig. 1a). The formation of iron oxide, for example, magnetite (Fe_3O_4),
206 usually involves the nucleation and growth process, but recently a rapid agglomeration of the
207 primary particles was also reported (Baumgartner et al., 2013). In the magnetic palygorskite
208 (Pal-IO), the spherical iron oxide particles were observed to accumulate along the fiber and

209 platy edge of the palygorskite (Fig. 1b and c). The precursor iron (Fe^{3+}/Fe^{2+}) supplied during
210 the synthesis reaction was assumed to diffuse along the negatively charged plane of
211 palygorskite. Since the palygorskite holds a permanent negative charge, the Coulombic
212 attraction would have driven the electrostatic interaction between the surface functional
213 groups of palygorskite and the oppositely charged Fe^{3+}/Fe^{2+} ions (Tombácz et al., 2001; Lee
214 et al., 2010) forming a crosslinking reaction between the clay surface and Fe (Chen et al.,
215 2016a). Thus, upon alkali addition (concentrated OH^-), the nucleation, growth and
216 agglomeration of iron oxide would occur primarily along the surface of palygorskite. The
217 estimated dimension of iron oxide particles in Pal-IO obtained through TEM images (Fig. 1c
218 and d) was between 15 to 25 nm. Although the fibrous particles of palygorskite were
219 randomly oriented, they still existed as bundles (approximate width: 100 to 130 nm) having
220 individual tubules (20 to 30 nm width) placed parallel to each other (Fig. 1c and 1d). These
221 observations showed that the strong interactions among the palygorskite particles were
222 preserved and their fiber-bundle design ensured a strong adherence towards the iron oxide
223 nanoparticles.
224

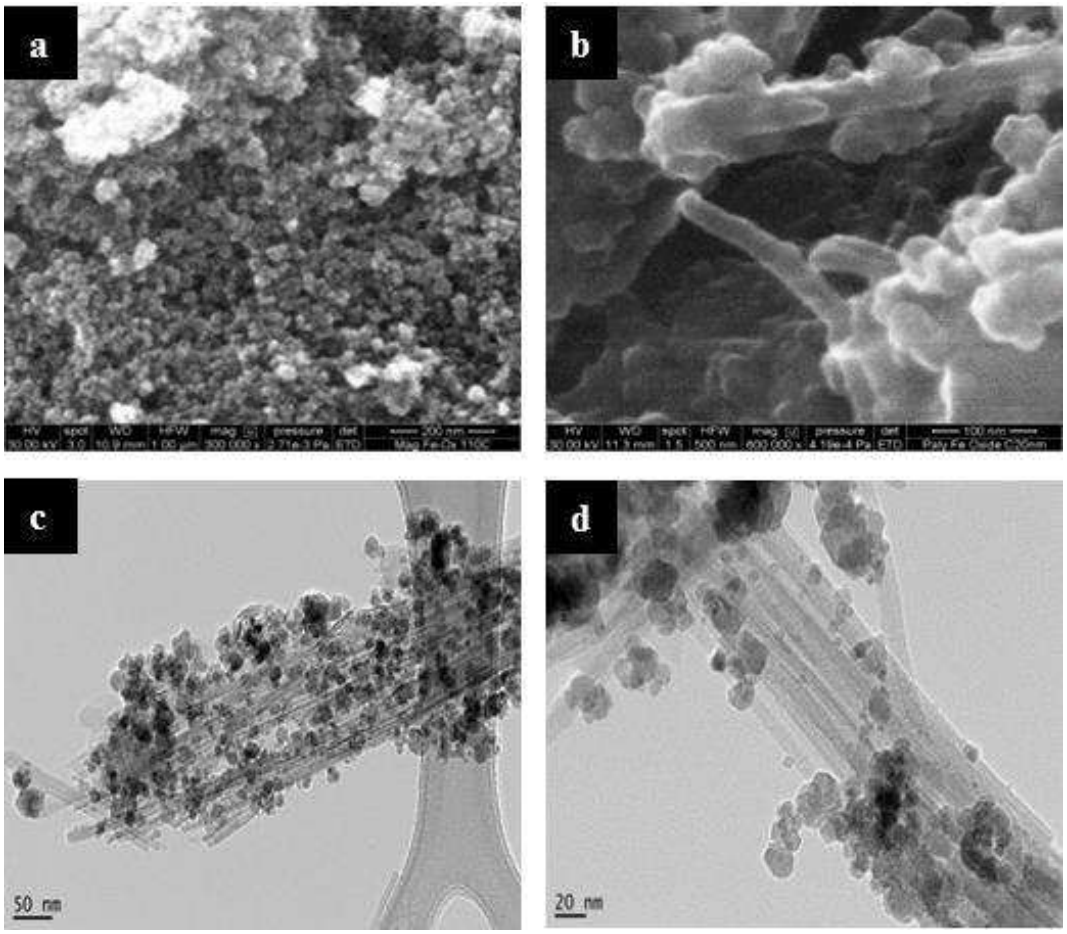

Fig. 1: SEM (a-b) and TEM (c-d) images of iron oxide and palygorskite-iron-oxide nanocomposite; (a) iron oxide, (b-d) palygorskite-iron oxide nanocomposite

The specific surface area (SSA) of the nanocomposite (Pal-IO) was significantly higher (99.8 $m^2 g^{-1}$) than the pristine materials (49.4 and 72.6 $m^2 g^{-1}$ for Pal and IO, respectively). All the materials exhibited a type IV adsorption profile (IUPAC classification) corresponding to mesoporous materials (Fig. 2a) (Sarkar et al., 2015). Both the palygorskite and Pal-IO had a hysteresis loop (H3 type) associated with the parallel plates or slit-shape pores (Sarkar et al., 2015), while iron oxide (IO) exhibited a H1 type loop with almost a consistent pore volume distribution (Fig. 2b). The increase of surface area and pore volume in Pal-IO was due to the leaching of cations and impurities from the clay matrix in the acidic Fe^{3+}/Fe^{2+} suspension (pH 2.2) (Section 2.2) that caused the rearrangement of clay mineral's porosity.

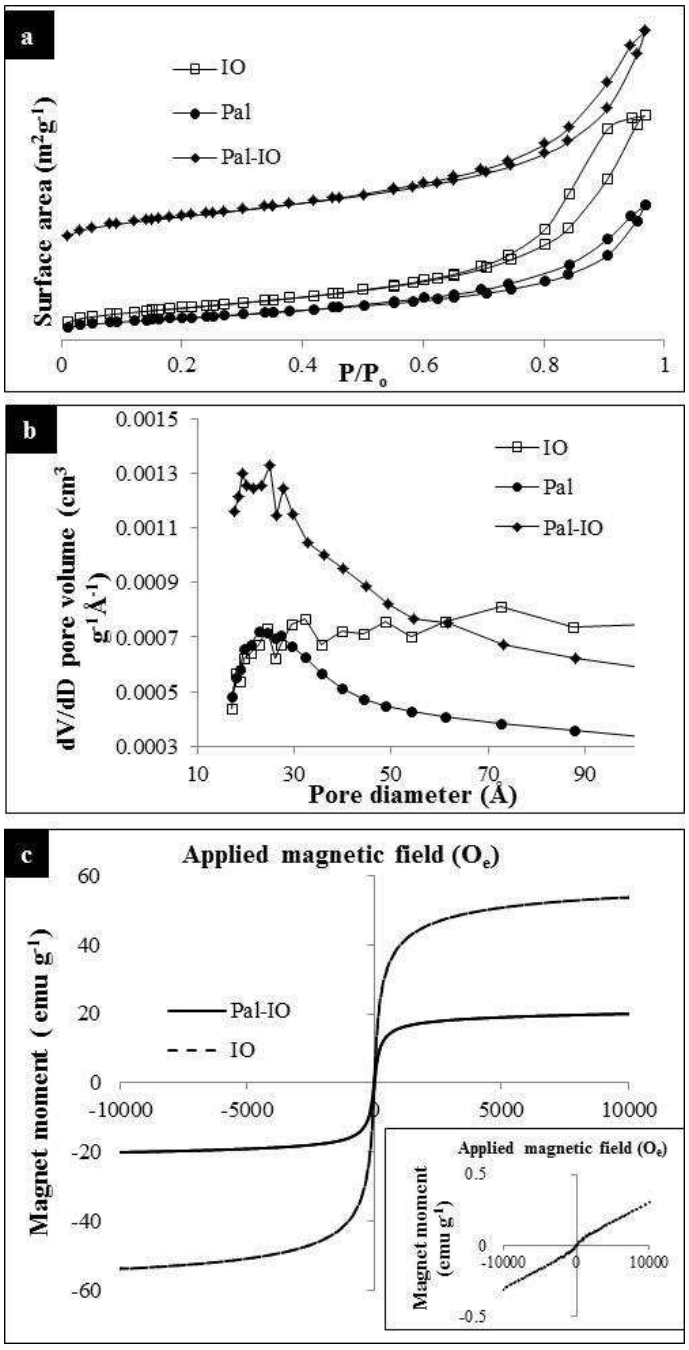

Fig. 2: N_2 adsorption-desorption isotherms (a), BJH pore size distribution (b), and magnetization curve (c) of palygorskite (Pal), iron oxide (IO) and palygorskite-iron oxide nanocomposite (Pal-IO). Inset in Fig.2 (c) is for palygorskite

The complete separation of Pal-IO from the suspension using Alnico magnet bar was generally fast (within 60 to 120 sec). The plot of M_s (emu g^{-1}) against the applied magnetic

field (O_e) of the iron oxide and Pal-IO produced an "S" shaped magnetic hysteresis loop with a near zero remanence and coercivity (Fig. 2c), which confirmed a superparamagnetic characteristic of the material (Tsuzuki et al., 2011). The bare iron oxide (IO) had the M_s value of 54.2 ± 2.5 emu g^{-1}. The slightly lower M_s value of the synthesized IO as compared to the bulk magnetite (Fe_3O_4) or maghemite (γ-Fe_2O_3) (92 and 87 emu g^{-1}, respectively) could be due to the formation of a thin layer of magnetically disordered shell on the nanoparticle surface (Tsuzuki et al., 2011). A M_s value of 20.2 ± 2.3 emu g^{-1} was recorded for the Pal-IO nanocomposite, which was higher than the recommended value for the conventional magnetic separation of a spent adsorbent (16.3 emu g^{-1}) (Ma et al., 2005). Meanwhile, palygorskite (Fig. 2c) was almost diamagnetic due to an extremely small magnetic saturation. The measured H_c for palygorskite and Pal-IO was 21.4 ± 3.1 and 18.8 ± 0.1 O_e (k A m^{-1}), respectively. The bare IO had a negligible H_c value. The appreciable decrease in the M_s value of Pal-IO as compared to the bare IO was due to the contribution of the nonmagnetic substance (palygorskite) (Liu et al., 2014).

The characteristic XRD reflections of palygorskite were observed at 2θ = 8.5° (10.39 Å), 19.6° (4.52 Å) and 24.9° (3.57 Å) together with the presence of kaolinite at 2θ = 12.3° (7.19 Å) and quartz at 2θ = 20.8° (4.27 Å) and 26.4° (3.37 Å) (Fig. 3a) (Sarkar et al., 2015). The sharp reflection at 2θ = 30.8° (Fig. 3a) was designated to dolomite (calcium magnesium carbonate) which was an impurity in the clay mineral sample. The synthesized iron oxide showed reflections at 2θ positions of 30.1°, 35.5°, 43.1° 53.4°, 57.0° and 62.6° (Fig. 3a) which respectively corresponded to (220), (311), (400), (422), (511) and (440) reflection planes of magnetite (Pan et al., 2011; Chen et al., 2016a). These diffraction patterns were in good agreement with the International Center for Diffraction Data (ICDD) reference pattern of magnetite (Fe_3O_4) (ICDD File No. 04-008-8146). In Pal-IO (Fig. 3a), a slight broadening of the (100) reflection of palygorskite (2θ = 8.5°) occurred, which suggested a mild reduction

271 in the palygorskite crystallinity due to their interaction with the iron oxide. Nevertheless, the
272 presence of all the characteristic palygorskite and Fe_3O_4 reflections in the Pal-IO diffraction
273 pattern (Fig. 3a) signified the successful deposition of the magnetic nanoparticles on the
274 palygorskite in Pal-IO.
275 In FTIR spectrum of palygorskite, (Fig. 3b), the –OH stretching vibration of Mg/Fe–OH
276 (3695 cm^{-1} and 3545 cm^{-1}), Al_2-OH (3618 cm^{-1}), Al-Al-OH (910 cm^{-1}) and Al-Mg-OH (880
277 cm^{-1}) represented the characteristic bands of this clay mineral (Madejová and Komadel, 2001;
278 Suárez and García-Romero, 2006). The silica structural confirmation appeared at 1030 cm^{-1}
279 (Si-O-Si asymmetric stretching), 790 cm^{-1} (Si-O-Si symmetric stretching) and 471 cm^{-1} (Si-
280 O-Si bending) bands. Meanwhile, the band at 578 cm^{-1} in the spectra of IO (magnetite) (Fig.
281 3b) corresponded to the stretching vibration of Fe-O together with a small maghemite (γ-
282 Fe_2O_3) band at 628 cm^{-1} (Namduri and Nasrazadani, 2008). The signature band positions that
283 corresponded to the palygorskite and iron oxide were present in the FTIR spectrum of Pal-IO
284 (Fig. 3b). However, the bands at 1450 cm^{-1} (C=O, carbonate impurity) (Gunasekaran et al.,
285 2006) , 3545 cm^{-1} (Mg-OH stretching), and 880 cm^{-1} (Al-Mg-OH bending) were diminished.
286

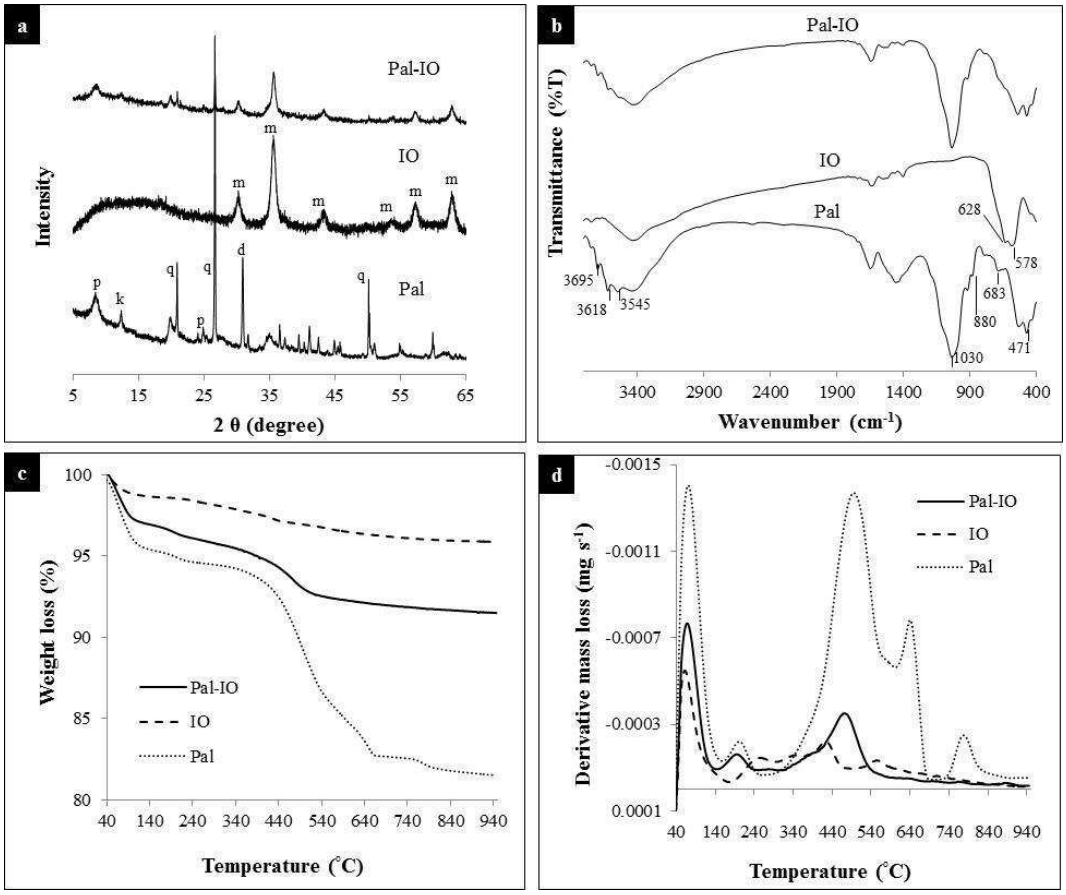

Fig. 3: Characteristic features of palygorskite (Pal), iron oxide (IO) and palygorskite-iron oxide nanocomposite (Pal-IO): (a) XRD patterns, (b) FTIR spectra, (c) TGA profiles and (d) DTGA profiles. (p = palygorskite, k = kaolinite, q = quartz, d = dolomite, m = magnetite)

In TGA, the magnetic nanocomposite (Pal-IO) displayed an 8.5% weight loss in the temperature range from 40 to 950°C (Fig. 3c) against 4% and 18% weight loss by bare iron oxide (IO) and pristine palygorskite (Pal), respectively. The palygorskite showed five pronounced endothermic weight loss steps (Fig. 3d): step 1 (4% loss with a peak at 65°C), step 2 (0.73% loss with a peak at 200°C), step 3 (9.8% loss with a peak at 503°C), step 4 (1.97% loss with a peak at 635°C) and step 5 (0.94% loss with a peak at 760°C). The step 1 was ascribed to the loss of surface-adsorbed and some zeolitic water. The step 2 was assigned to the elimination of the remaining zeolitic water. The dehydration and loss of the bound water were assigned to step 3 (Cheng et al., 2011). The step 4 and step 5 could possibly

correspond to the dolomite or calcite decarbonation (Guggenheim and Groos, 2001; Cheng et al., 2011) and dehydroxylation of structural Mg-OH groups (Frost and Ding, 2003), respectively. In Pal-IO, only three weight loss steps were observed (peaks at 48°C, 180°C and 465°C) (Fig. 3d), which corresponded to the elimination of various types of waters either from the palygorskite exterior surface or internal structure, as explained above for pristine palygorskite. The disappearance of peaks at step 4 and 5 in Pal-IO thermogram suggested dolomite/calcite decarbonation and dehydroxylation, respectively (as also observed in case of pristine palygorskite).

Overall findings in the characterization studies confirmed the integration of the pristine material (palygorskite and iron oxide) in Pal-IO. The composite showed better structural properties like higher SSA, more thermally stable, and better magnetic responsiveness. A successful removal of carbonate impurity from the palygorskite (as confirmed by XRD, FTIR and TGA) was achieved as a consequence of its dispersion in an acidic Fe^{3+}/Fe^{2+} solution during the synthesis process. This protocol therefore was able to exclude the conventional pre-treatment steps of clay minerals (using inorganic acids like HCl or HNO_3) for a greener and cost-effective synthesis.

3.2 Adsorption of Pb(II)

3.2.1 Adsorption isotherm

The theoretical interpretation of the relationship between adsorption capacity and equilibrium concentration was done using two well-established isothermal models, namely the Langmuir and Freundlich model (Supporting Information: S1). In a preliminary experiment, the maximum Pb(II) removal by Pal-IO was achieved at pH 5 (Supporting Information: SI Fig. 1), thus this pH value was used throughout the isothermal studies. The pH 5 is also a typical pH associated with contaminated waters from gold and coal mining activities (Lottermoser,

2010). The adsorption isotherm data of Pal-IO and Pal (Fig. 4a) exhibited a very sharp "elbow" at the equilibrium concentration (C_e) less than 50 mg L^{-1} (which corresponded to the initial concentration of 10 to 200 mg L^{-1}). It was followed by a steady increase up to C_e of 100 mg L^{-1}. The shape resembled an H type (Giles classification) isotherm associated with an almost complete adsorption due to a very high affinity of solute (Pb(II)) towards the adsorbent (Giles et al., 1960).

The adsorption data for IO, Pal and Pal-IO best fitted to the Langmuir model (regression coefficient, $R^2 > 0.98$; $p < 0.05$) (Table 1 and Supporting Information: SI Fig. 2), which suggested a monolayer adsorption on the active sites of each adsorbent. The palygorskite (Pal) showed the highest monolayer saturation capacity (q_{max}); Pal-IO had the highest K_L value which demonstrated a stronger interaction of their active sites (e.g., Al-O^-, Si-O^- or Fe-O^-) with Pb(II). These findings were in accordance with the higher n value (favorability of adsorption) for Pal-IO derived from the Freundlich isothermal model (Table 1). The calculated R_L values at all concentration for each adsorbent recorded a value between 0 and 1 (Supporting Information: SI Table 1), which again signified a favorable adsorption reaction.

Table 1: Isothermal and kinetic model fitting parameters for the adsorption of Pb(II) on palygorskite, iron oxide and palygorskite-iron oxide nanocomposite (at 25°C, under 150 agitation min^{-1} with 5 g L^{-1} adsorbent loading)

Model	Parameter	Palygorskite	Iron oxide	Palygorskite-iron oxide nanocomposite
Isothermal models				
Langmuir	q_{max} (calculated) (mg g^{-1})	50.8	6.00	26.7
	K_L (L mg^{-1})	0.136	0.040	0.303

	q_{max} (experimental) (mg g^{-1})	49.2	6.10	26.6
	R^2	0.9992	0.9896	0.9995
Freundlich	K_F (L g^{-1})	6.852	1.097	6.566
	n	2.30	3.43	3.47
	q_{max} (calculated) (mg g^{-1})	37.3	1.80	16.9
	R^2	0.8762	0.9831	0.8588
Kinetic models				
Pseudo first order	k_1 (min^{-1})	[a]NS	NS	0.035
	q_{max} (calculated) (mg g^{-1})	NS	NS	2.8
	q_{max} (experimental) (mg g^{-1})	NS	NS	4.1
	R^2	NS	NS	0.8947
Pseudo second order	k_2 (g mg^{-1} min^{-1})	NS	NS	0.012
	q_{max} (calculated) (mg g^{-1})	NS	NS	4.4
	q_{max} (experimental) (mg g^{-1})	NS	NS	4.1
	R^2	NS	NS	0.9945
Intra particle diffusion	k_i (mg g^{-1} $min^{0.5}$)	NS	NS	0.2071
	R^2	NS	NS	0.8249

[a] NS = not studied.

348 The adsorption profiles of the pristine palygorskite and iron oxide were useful to understand
349 the relationship and contribution of each individual component towards the adsorption
350 characteristic of the nanocomposite. In an aqueous system, iron oxide (magnetite) would
351 hydrate to form a Fe-OH coating layer surrounding the particles. Depending on the pH of the
352 aqueous solution, the Fe-OH layer could develop either a positive or negative surface charge
353 with the available H^+ or OH^- (Illés and Tombácz, 2006). As the isoelectric point (IEP) of IO
354 was 5.6 (Supporting Information: SI Fig. 3), at the given experimental conditions (pH 5), the
355 IO had a positively charged surface below pH 5.6. Therefore, IO had less affinity to Pb(II),
356 which further explained its poor adsorption capacity (Table 1). Furthermore, the bare iron
357 oxide nanoparticles were prone to aggregation due to their high surface energy that later
358 reduced the Pb(II) accessibility towards active sites (Chen et al., 2016b). Meanwhile, the
359 pristine palygorskite showed a high adsorption capacity owing to their negative surface
360 charge that resembled the abundance of active sites for interaction with Pb(II). In general, the
361 adsorption of cationic metal on clay minerals can occur though both specific and non-specific
362 adsorption. The non-specific adsorption (outer sphere complexation) involves the cation
363 exchange reaction within the interlayer, while the specific adsorption (inner sphere
364 complexation) often occurs through the silanol and aluminol groups at the edges of clay
365 particles (El-Bayaa et al., 2009).
366 In the case of Pal-IO, the nanocomposite showed an appreciable decrease in the maximum
367 adsorption capacity (q_{max}) in comparison to the pristine palygorskite (Pal) (Table 1).
368 However, when considering the K_L, n and R_L values (Table 1 and Supporting Information: SI
369 Table 1), Pal-IO showed a stronger affinity towards Pb(II) as compared to both Pal and IO.
370 As shown in the gray scale area (Fig. 4b), at initial Pb(II) concentration between 10 to 200
371 mg L^{-1}, Pal-IO showed a higher adsorption capacity than Pal and IO (up to 63% and 86%
372 more, respectively). The greater adsorption capacity was contributed by the higher pore

volume of Pal-IO as compared to Pal (Fig. 2b), which allowed more Pb(II) diffusion towards the active sites of the nanocomposite. In addition, the synergic contribution of the active sites from both parent materials, e.g., silanol (Si-OH) and aluminol (Al-OH) functional groups in Pal and $Fe\text{-}O^-$ in IO, could possibly enhance the composite's affinity towards the heavy metal cation. Clay minerals like palygorskite may have variable surface charges constituted of Si-OH and Al-OH groups that are capable to adsorb metal cations through inner-sphere complexation depending on the system pH (El-Bayaa et al., 2009). Meanwhile, $Fe\text{-}O^-$ could act as a Lewis base by coordinating with Pb^{2+} to form inner-sphere complexes (Kumari et al., 2015). At the working pH 5, partial protonation of $Fe\text{-}O^-$ to Fe-OH could also lead to both inner- and outer-sphere complexations with Pb^{2+} (Kumari et al., 2015).

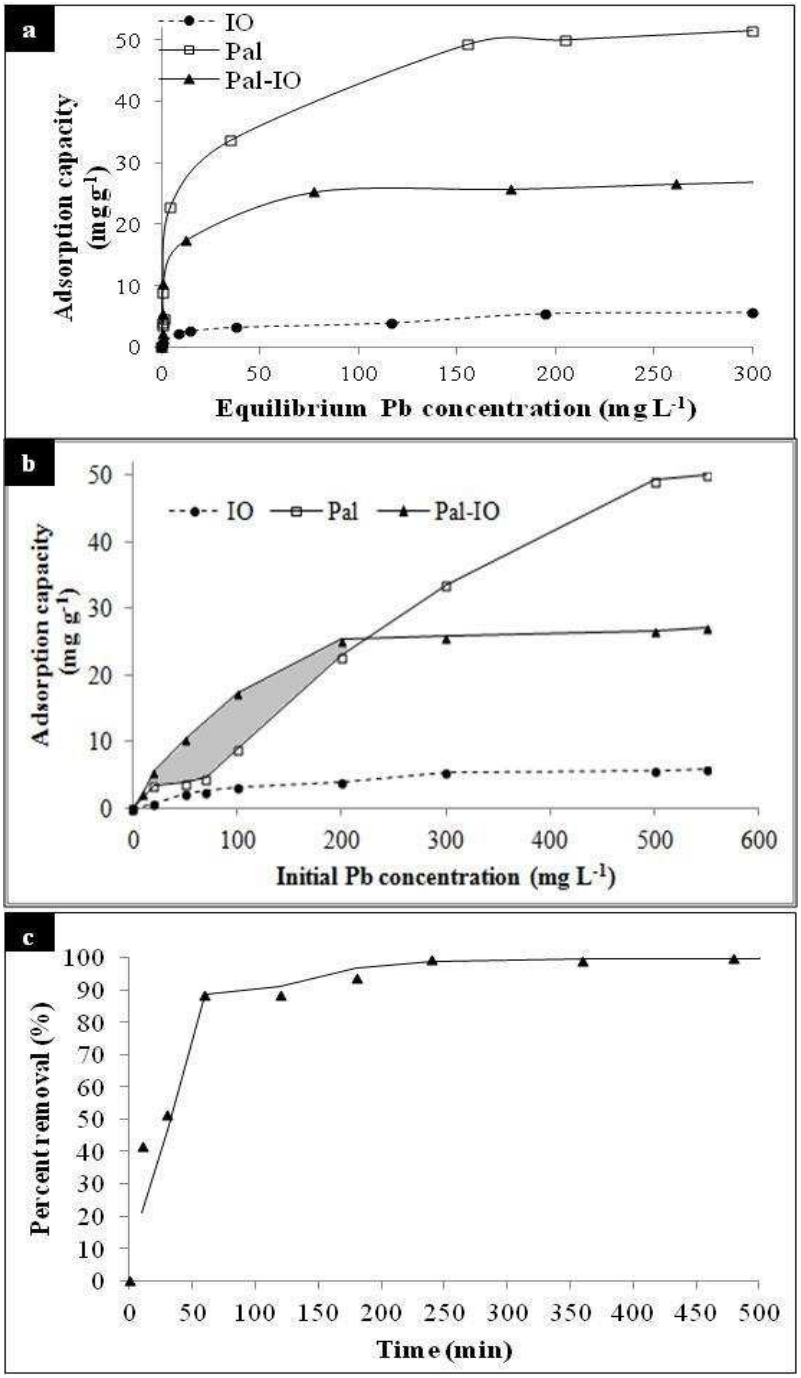

Fig. 4: Adsorption of Pb(II) on palygorskite (Pal), iron-oxide (IO) and palygorskite-iron oxide nanocomposite (Pal-IO): (a) adsorption isotherms, (b) effect of initial Pb(II) concentration on the adsorption capacity, and (c) effect of reaction time on Pb(II) removal by Pal-IO at initial Pb(II) concentration of 50 mg L^{-1} at 25°C with 150 agitations min^{-1} and 5 g L^{-1} loading

391 3.2.2 Adsorption kinetics

392 The pseudo-first order, pseudo-second order and intra-particle diffusion models were chosen
393 to establish an understanding of the adsorption kinetics (Supporting Information: SI 2). The
394 kinetic plot (Fig. 4c) showed that 42% of Pb(II) was removed in the first 10 min of the
395 experiment, double (89%) at 60 min of reaction, and full equilibrium (~100%) after 240 min.
396 The relatively faster reaction rate indicated a high affinity of Pb(II) towards the active sites of
397 Pal-IO, in accordance with the observed H type adsorption isotherm (Section 3.2.1). To
398 ensure a complete equilibrium at various initial concentrations, a 12 h equilibration time was
399 therefore necessary. Among the three kinetic models applied, the pseudo-second order model
400 most suited the adsorption data ($R^2 = 0.9945$; $p < 0.05$), where the q_{max} value was consistent
401 with the experimental value (Table 1). The fitness of the pseudo-second order model
402 indicated that the rate limiting step of Pb(II) adsorption occurred through chemisorption (Ho
403 and McKay, 1999).

404

405 3.3 Desorption studies

406 3.3.1 Effect of desorbing agent

407 At given experimental conditions, the type of desorbing agent and pH was found to
408 significantly influence the desorption of Pb(II) from Pal-IO (Table 2). The negligible Pb(II)
409 desorption in Milli-Q water (pH 6.2) reflected the high retention ability of Pb(II) by the
410 nanocomposite. In acidic solutions, the lower pH could enhance the metal desorption due to
411 the leaching of cations (e.g., Fe). At 0.01 M concentration, HCl showed a higher release of
412 Pb(II) compared to HNO_3, but the trend was reversed at 0.1 M concentration. The chloride
413 ions in HCl were able to form effective complexes with Pb(II) to assist the desorption process
414 (Kim et al., 2011). However, at a higher acid concentration, HNO_3 might cause the oxidation
415 of magnetite (Mandel et al., 2011) in Pal-IO that likely would disrupt the composite's

stability to hold Pb(II). The increase in pH of the acidic desorbing agent following the desorption reaction also suggested a possible cation exchange between H^+ with Pb(II) at the active sites (Huang et al., 2007).

Table 2: Desorption of Pb(II) from Pal-IO using various desorbing agents (standard error at 0.95 confidence level)

Desorbing agent	Initial pH	Final pH	Desorption (%)	Fe leached (%)
0.01 M HCl	1.96	2.21	89.2±7.23	0.57
0.1 M HCl	1.57	4.54	75.6±1.90	2.89
0.01 M NaOH	11.3	10.8	0.55±0.55	0.88
0.01 M NaCl	5.16	5.99	1.20±0.02	ND[b]
0.01 M NH_4OAc (ammonium acetate)	6.67	3.54	0.45±0.24	ND
Milli-Q water	6.20	6.47	0.78±0.23	ND
0.01 M HNO_3	1.80	4.48	72.0±1.25	0.42
0.1 M HNO_3	1.66	4.75	90.4±1.70	2.61

0.01 M EDTA-Na_2	8.90	4.62	95.0±3.14	0.78
0.1 M EDTA-Na_2	9.10	4.52	95.57±0.10	0.88

422

423 [b] ND = not detected.

424

425 Ammonium acetate is commonly used to determine the cation exchange capacity (CEC) of
426 clay minerals where NH_4^+ can be easily exchanged with the cationic species present in the
427 interlayer. A very small Pb(II) desorption by ammonium acetate in the desorption test
428 indicated that, (i) Pb(II) might not be exchangeable with other cations at the interlayer region,
429 and (ii) if Pb(II) was present in the interlayer, NH_4^+ might not be able to replace Pb(II) due to
430 some steric hindrance of NH_4^+ tetrahedral configuration and larger ionic radii (1.48 Å) as
431 compared to Pb(II) (1.32 Å) (Shahbazi et al., 2013). On the other hand, smaller cations like
432 Na^+ (ionic radius of 0.95 Å) in NaCl might be easily exchangeable with Pb(II).
433 EDTA usually showed a higher metal desorption over inorganic acids due to its ability to
434 form strong complexation (up to six coordination indexes) via the electron rich (amidogen
435 and carboxylic) ligand groups (Huang et al., 2007). The recorded pH reduction (Table 2)
436 signified the release of proton (H^+) from the hydroxyl groups within EDTA that were used up
437 during Pb(II) complexation. Both 0.01 and 0.1 M EDTA-Na_2 showed a high Pb(II) desorption
438 (more than 90%). In contrast to HCl and HNO_3, the amount of Fe leached out from Pal-IO
439 using EDTA was negligible (4.41 mg L^{-1}; <1%) even at a 0.1 M concentration (Table 2).
440 Considering the desorptive effectiveness of Pb(II) and economic perspective, 0.01 M EDTA-
441 Na_2 was preferably the best desorbing agent. However, HCl might also have some advantages
442 in terms of cheaper cost and availability. The percentage of Fe leached from Pal-IO by 0.01

M HCl and 0.01 M EDTA-Na_2 was only 0.57 and 0.78%, respectively (Table 2). Thus, the leached Fe was considered to have insignificant effect towards Pb(II) adsorption capabilities of the composite.

3.3.2 Regeneration of the adsorbent

The regeneration cycle of Pal-IO was carried out by using both EDTA and HCl as the desorbing agent. For better clarification, the Pb(II) loaded Pal-IO, which was desorbed by 0.01 M EDTA-Na_2 and 0.01 M HCl, were assigned as Pal-IO-EDTA and Pal-IO-HCl, respectively. The Pb(II) removal during desorption with EDTA was reduced by 21.3 and 31.2% after the second and third cycle, respectively (Fig. 5a). A small portion of Pb(II) might strongly bind to the nanocomposite as indicated by the 97.5% desorption using EDTA in the first cycle (Fig. 5a). By making an assumption that 26.6 mg g^{-1} Pb(II) loading (calculated q_{max} based on the Langmuir model; Table 1) would make 100% monolayer coverage, the initial concentration of 100 mg L^{-1} would make 65% coverage at each adsorption cycle. Thus, during the second and third cycle the active sites became extensively occupied with the freshly supplied Pb(II) together with the remaining Pb(II) entrapped in the prior cycle(s). This factor thus resulted in a lower Pb(II) adsorption in the subsequent cycles. The findings were also in parallel with a slight increase in Pb(II) desorption at the second and third cycle (Fig.5a). The excess build-up of Pb(II) within the nanocomposite could stimulate its release during desorption as the saturated nanocomposite could no longer hold the additional Pb(II). Meanwhile, the adsorption-desorption cycle of Pal-IO showed a similar pattern when using HCl as the desorbing agent. However, the adsorption by Pal-IO-HCl was greatly reduced from 97% (first cycle) to 50 and 48% in the second and third cycle, respectively.

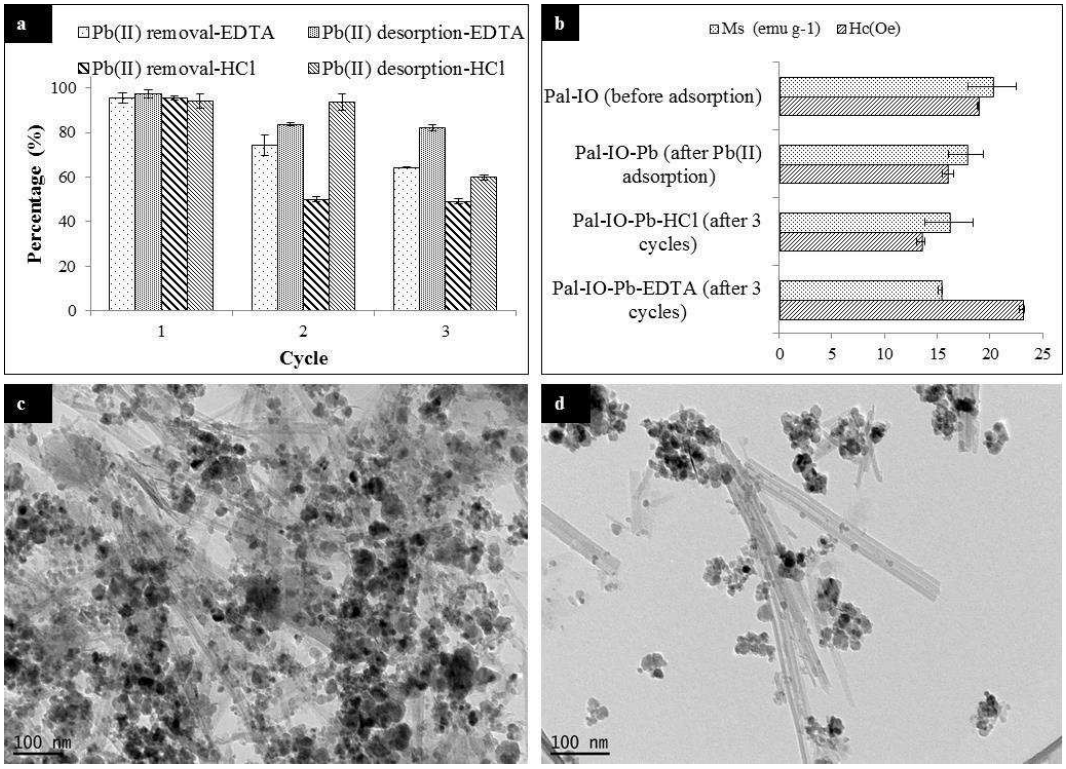

Fig. 5: Comparison on Pb(II) adsorption and desorption (in percentage) by Pal-IO using EDTA (Pal-IO-EDTA) and HCl (Pal-IO-HCl) as the desorbing agent (a), magnetic properties of fresh and spent Pal-IO nanocomposite (b), and TEM images of Pal-IO-EDTA (c) and Pal-IO-HCl (d) nanocomposite after three regeneration cycles. Error bars represent the standard error at 0.95 confidence level.

The findings of the adsorption-desorption cycles were correlated with the changes observed in the magnetic properties of the spent Pal-IO at three different stages; (i) before Pb(II) adsorption, (ii) after Pb(II) adsorption, and (iii) after three adsorption-desorption cycles (Fig. 5b). After third regeneration cycle, Pal-IO-EDTA showed a higher magnitude of coercivity (H_c) than Pal-IO-HCl (Fig. 5b), which suggested that the solid aggregation was greater in the earlier material. It was reported that EDTA was able to produce strong complexes with iron (hydr)oxide (Fe-EDTA complexes) that simultaneously promoted their dissolution from Pal-IO due to weakened surface Fe-O bonds (Norén et al., 2009). The Fe-EDTA complexes

might readsorb on the Fe-O surface as previously found in goethite (α-FeOOH) (Norén et al., 2009). Therefore, the dissolution-readsorption of Fe-EDTA complexes could possibly occur through the embedded iron oxide nanoparticles within the Pal-IO nanocomposite, which later influenced the coercivity due to the changes in surface properties and shape anisotropy (Issa et al., 2013). Each material showed almost equivalent magnetic susceptibility (M_s) with a reduction of 4.0 to 4.8 from the original value (20.2 emu g^{-1}) (Fig. 5b). A minor loss of M_s indicated that iron oxide nanoparticles were strongly adhered to the palygorskite. This conclusion was supported by the TEM images of the spent Pal-IO (Fig. 5c and 5d). In Pal-IO-EDTA (Fig. 5c), majority of the iron oxide nanoparticles were still closely adhered to the palygorskite bundles even after the three consecutive regeneration cycles. In contrast, the palygorskite fibers were seen detached from their bundles in Pal-IO-HCl (Fig. 5d) accompanied by some scattered iron oxide nanoparticles. Therefore, it could be concluded that the acidic treatment for desorption had the potential to disaggregate the particles in spent Pal-IO nanocomposite to make it more loosely packed. This observation was useful to explain the reduction in Pb(II) adsorption in the regeneration profile of Pal-IO-HCl. Acid attack on clay minerals could cause hydrolysis and dissolution of octahedral layers at the edges. Thus, repeated desorption of spent Pal-IO with HCl would possibly expedite palygorskite's dissolution, which might lead to disaggregation of the crystal bundles of the clay mineral. Additionally, some entrapped H^+ (from HCl) within the Pal-IO matrix could reduce the availability of active sites for Pb^{2+}, and thus decrease the metal's adsorption in the next regeneration cycles. These hypotheses however require further investigation to prove. The overall findings demonstrated that the choice of desorbing agent influenced the magnetic recyclability and metal leaching from Pal-IO. For future prospective application of Pal-IO in waste water remediation, EDTA would be a more preferable desorbing agent over HCl, as also proposed previously (Udovic and Lestan, 2012).

3.3.3 Environmental implication

The superparamagnetic Pal-IO composite described in this study could be implemented for remediating heavy metals from contaminated wastewaters in a treatment plant. Due to advantages like low costs, simple preparatory steps, high specific surface area and large adsorption capacities, Pal-IO is expected to be a promising material in removing Pb and other heavy metals (e.g., Cr and Cd) from waste waters (Kumari et al., 2015). The Pb(II) removal capacity of Pal-IO is comparable to some reported adsorbents, such as mesoporous magnetite nanospheres (Brigante et al., 2016), functionalized mesoporous silica (Shahbazi et al., 2013), and magnetic Fe_3O_4/halloysite composite (Tian et al., 2016). According to the existing findings, the material might fit to treat wastewaters which contain a typical Pb(II) concentration up to 200 mg L^{-1}. However, further research is needed to assess the material's Pb(II) removal efficiency in the presence of other co-existing heavy metals. Desorption with EDTA makes the spent material fit for potential reuse over a greater number of cycles than an acid treatment, but disposal of the Pb-EDTA might pose a secondary environmental issue because of the strong binding strength in the metal-EDTA complex. This may potentially be addressed by alkali (Kim and Ong, 1999) precipitation of the concerned solution, but further research is necessary to better understand and address these issues.

4. Conclusions

Palygorskite-iron oxide nanocomposite was successfully synthesized by a co-precipitation method and applied as an adsorbent of aqueous Pb(II). Pal-IO exhibited a high specific surface area (99.8 $m^2 g^{-1}$), low isoelectric point (3.5) and significant magnetic susceptibility (20.2 emu g^{-1}) that facilitated its potential application as an adsorbent for removing Pb(II). The maximum Pb(II) adsorption capacity of 26.6 mg g^{-1} at pH 5 was achieved for the

treatment of contaminated water containing up to 200 mg L^{-1} Pb(II). EDTA-Na_2 was the best desorbing agent for regenerating the magnetic adsorbent with more than 90% desorption capability. Three consecutive adsorption-desorption cycles yielded more than 64% removal of Pb(II) at the end. The strong binding of iron oxide nanoparticles on palygorskite, the nanocomposite's superior magnetic properties and the least leaching of iron verified the magnetic stability and recyclability of Pal-IO. The nanocomposite could emerge as a promising material for purifying wastewaters contaminated especially with heavy metal cations.

Acknowledgments

This study was partially supported by the Clay Minerals Society (CMS) Student Research Grant (2016). Ruhaida Rusmin acknowledges the Ministry of Higher Education of Malaysia and Universiti Teknologi MARA for the PhD scholarship award. The authors acknowledge Dr Xiang Zhao from the Earth Environment Paleomagnetism Laboratory, Australian National University, for assistance with the VSM measurement, and Mr. Stuart McClure (University of South Australia) for the SEM analysis.

References

Ambashta, R.D., Sillanpää, M., 2010. Water purification using magnetic assistance: A review. Journal of Hazardous Materials 180, 38-49.

ATSDR, 2015. Agency for Toxic Substances and Disease Registry (ATSDR), Substance Priority List 2015. U.S. Department of Health and Human Services, USA.

Baumgartner, J., Dey, A., Bomans, P.H.H., Le Coadou, C., Fratzl, P., Sommerdijk, N.A.J.M., Faivre, D., 2013. Nucleation and growth of magnetite from solution. Nature Materials 12, 310-314.

Brigante, M., Pecini, E., Avena, M., 2016. Magnetic mesoporous silica for water remediation: Synthesis, characterization and application as adsorbent of molecules and ions of environmental concern. Microporous and Mesoporous Materials 230, 1-10.

Chen, J., Yan, L.-g., Yu, H.-q., Li, S., Qin, L.-l., Liu, G.-q., Li, Y.-f., Du, B., 2016b. Efficient removal of phosphate by facile prepared magnetic diatomite and illite clay from aqueous solution. Chemical Engineering Journal 287, 162-172.

Chen, L., Zhou, C.H., Fiore, S., Tong, D.S., Zhang, H., Li, C.S., Ji, S.F., Yu, W.H., 2016a. Functional magnetic nanoparticle/clay mineral nanocomposites: preparation, magnetism and versatile applications. Applied Clay Science 127–128, 143-163.

Cheng, H., Yang, J., Frost, R.L., 2011. Thermogravimetric analysis-mass spectrometry (TG-MS) of selected Chinese palygorskites—Implications for structural water. Thermochimica Acta 512, 202-207.

El-Bayaa, A.A., Badawy, N.A., AlKhalik, E.A., 2009. Effect of ionic strength on the adsorption of copper and chromium ions by vermiculite pure clay mineral. Journal of Hazardous Materials 170, 1204-1209.

Frost, R.L., Ding, Z., 2003. Controlled rate thermal analysis and differential scanning calorimetry of sepiolites and palygorskites. Thermochimica Acta 397, 119-128.

Giles, C.H., MacEwan, T.H., Nakhwa, S.N., Smith, D., 1960. Studies in adsorption. Part XI. A system of classification of solution adsorption isotherms, and its use in diagnosis of adsorption mechanisms and in measurement of specific surface areas of solids. Journal of the Chemical Society (Resumed), 3973-3993.

Guggenheim, S., Groos, A.F.K.V., 2001. Baseline studies of the Clay Minerals Society source clays: thermal analysis. Clays and Clay Minerals 49.

Gunasekaran, S., Anbalagan, G., Pandi, S., 2006. Raman and infrared spectra of carbonates of calcite structure. Journal of Raman Spectroscopy 37, 892-899.

582 Han, Y., Cao, X., Ouyang, X., Sohi, S.P., Chen, J., 2016. Adsorption kinetics of magnetic
583 biochar derived from peanut hull on removal of Cr (VI) from aqueous solution:
584 Effects of production conditions and particle size. Chemosphere 145, 336-341.
585 Harvey, P.J., Handley, H.K., Taylor, M.P., 2015. Identification of the sources of metal (lead)
586 contamination in drinking waters in north-eastern Tasmania using lead isotopic
587 compositions. Environmental Science and Pollution Research 22, 12276-12288.
588 Ho, Y.S., McKay, G., 1999. Pseudo-second order model for sorption processes. Process
589 Biochemistry 34, 451-465.
590 Huang, M.-R., Lu, H.-J., Li, X.-G., 2007. Efficient multicyclic sorption and desorption of
591 lead ions on facilely prepared poly(m-phenylenediamine) particles with extremely
592 strong chemoresistance. Journal of Colloid and Interface Science 313, 72-79.
593 Illés, E., Tombácz, E., 2006. The effect of humic acid adsorption on pH-dependent surface
594 charging and aggregation of magnetite nanoparticles. Journal of Colloid and Interface
595 Science 295, 115-123.
596 Issa, B., Obaidat, I.M., Albiss, B.A., Haik, Y., 2013. Magnetic Nanoparticles: Surface Effects
597 and Properties Related to Biomedicine Applications. International Journal of
598 Molecular Sciences 14, 21266-21305.
599 Kim, C., Ong, S.-K., 1999. Recycling of lead-contaminated EDTA wastewater. Journal of
600 Hazardous Materials 69, 273-286.
601 Kim, K.-J., Kim, D.-H., Yoo, J.-C., Baek, K., 2011. Electrokinetic extraction of heavy metals
602 from dredged marine sediment. Separation and Purification Technology 79, 164-169.
603 Kumari, M., Pittman, C.U., Mohan, D., 2015. Heavy metals [chromium (VI) and lead (II)]
604 removal from water using mesoporous magnetite (Fe_3O_4) nanospheres. Journal of
605 Colloid and Interface Science 442, 120–132.

606 Lee, P.-L., Chiu, Y.-K., Sun, Y.-C., Ling, Y.-C., 2010. Synthesis of a hybrid material
607 consisting of magnetic iron-oxide nanoparticles and carbon nanotubes as a gas
608 adsorbent. Carbon 48, 1397-1404.
609 Lottermoser, B. G., 2010. Mine Water. In: Lottermoser, B. G. (3rd Ed.). Mine Wastes.
610 Springer Berlin Heidelberg, pp. 119–203.
611 Liu, H., Chen, W., Liu, C., Liu, Y., Dong, C., 2014. Magnetic mesoporous clay adsorbent:
612 Preparation, characterization and adsorption capacity for atrazine. Microporous and
613 Mesoporous Materials 194, 72-78.
614 Ma, Z., Guan, Y., Liu, H., 2005. Synthesis and characterization of micron-sized
615 monodisperse superparamagnetic polymer particles with amino groups. Journal of
616 Polymer Science Part A: Polymer Chemistry 43, 3433-3439.
617 Madejová, J., Komadel, P., 2001. Baseline studies of the clay minerals society source clays:
618 infrared methods. Clays and Clay Minerals 49, 410-432.
619 Mahdavian, A.R., Mirrahimi, M.A.-S., 2010. Efficient separation of heavy metal cations by
620 anchoring polyacrylic acid on superparamagnetic magnetite nanoparticles through
621 surface modification. Chemical Engineering Journal 159, 264-271.
622 Mandel, K., Hutter, F., Gellermann, C., Sextl, G., 2011. Synthesis and stabilisation of
623 superparamagnetic iron oxide nanoparticle dispersions. Colloids and Surfaces A:
624 Physicochemical and Engineering Aspects 390, 173-178.
625 Murray, H.H., 2006. Chapter 2 Structure and Composition of the Clay Minerals and their
626 Physical and Chemical Properties. in: Haydn, H.M. (Ed.). Developments in Clay
627 Science. Elsevier, pp. 7-31.
628 Naidu, R., 2013. Recent advances in contaminated site remediation. Water, Air, & Soil
629 Pollution 224, 1705.

630 Namduri, H., Nasrazadani, S., 2008. Quantitative analysis of iron oxides using Fourier
631 transform infrared spectrophotometry. Corrosion Science 50, 2493-2497.
632 Norén, K., Loring, J.S., Bargar, J.R., Persson, P., 2009. Adsorption mechanisms of EDTA at
633 the water−iron oxide interface: implications for dissolution. The Journal of Physical
634 Chemistry C 113, 7762-7771.
635 Pan, J., Xu, L., Dai, J., Li, X., Hang, H., Huo, P., Li, C., Yan, Y., 2011. Magnetic molecularly
636 imprinted polymers based on attapulgite/Fe3O4 particles for the selective recognition
637 of 2,4-dichlorophenol. Chemical Engineering Journal 174, 68-75.
638 Sarkar, B., Liu, E., McClure, S., Sundaramurthy, J., Srinivasan, M., Naidu, R., 2015.
639 Biomass derived palygorskite–carbon nanocomposites: Synthesis, characterisation
640 and affinity to dye compounds. Applied Clay Science 114, 617-626.
641 Sarkar, B., Xi, Y.F., Megharaj, M., Krishnamurti, G.S.R., Bowman, M., Rose, H., Naidu, R.,
642 2012. Bioreactive organoclay: a new technology for environmental remediation.
643 Critical Reviews in Environmental Science and Technology 42, 435-488.
644 Shahbazi, A., Younesi, H., Badiei, A., 2013. Batch and fixed-bed column adsorption of
645 Cu(II), Pb(II) and Cd(II) from aqueous solution onto functionalised SBA-15
646 mesoporous silica. The Canadian Journal of Chemical Engineering 91, 739-750.
647 Su, C., 2017. Environmental implications and applications of engineered nanoscale magnetite
648 and its hybrid nanocomposites: A review of recent literature. Journal of Hazardous
649 Materials 322, Part A, 48-84.
650 Suárez, M., García-Romero, E., 2006. FTIR spectroscopic study of palygorskite: Influence of
651 the composition of the octahedral sheet. Applied Clay Science 31, 154-163.
652 Tian, X., Wang, W., Tian, N., Zhou, C., Yang, C., Komarneni, S., 2016. Cr(VI) reduction and
653 immobilization by novel carbonaceous modified magnetic Fe3O4/halloysite
654 nanohybrid. Journal of Hazardous Materials 309, 151-156.

655 Tombácz, E., Csanaky, C., Illés, E., 2001. Polydisperse fractal aggregate formation in clay
656 mineral and iron oxide suspensions, pH and ionic strength dependence. Colloid and
657 Polymer Science 279, 484-492.
658 Tombácz, E., Turcu, R., Socoliuc, V., Vékás, L., 2015. Magnetic iron oxide nanoparticles:
659 Recent trends in design and synthesis of magnetoresponsive nanosystems.
660 Biochemical and Biophysical Research Communications 468(3), 442–453.
661 Tsuzuki, T., Schäffel, F., Muroi, M., McCormick, P.G., 2011. Magnetic properties of
662 mechanochemically synthesized γ-Fe2O3 nanoparticles. Journal of Alloys and
663 Compounds 509, 5420-5425.
664 Udovic, M., Lestan, D., 2012. EDTA and HCl leaching of calcareous and acidic soils
665 polluted with potentially toxic metals: Remediation efficiency and soil impact.
666 Chemosphere 88, 718-724.
667 Xiang, B., Fan, W., Yi, X., Wang, Z., Gao, F., Li, Y., Gu, H., 2016. Dithiocarbamate-
668 modified starch derivatives with high heavy metal adsorption performance.
669 Carbohydrate Polymers 136, 30-37.
670 Xu, P., Zeng, G.M., Huang, D.L., Feng, C.L., Hu, S., Zhao, M.H., Lai, C., Wei, Z., Huang,
671 C., Xie, G.X., Liu, Z.F., 2012. Use of iron oxide nanomaterials in wastewater
672 treatment: A review. Science of The Total Environment 424, 1-10.
673 Yoshida, A., Terazono, A., Ballesteros Jr, F.C., Nguyen, D.-Q., Sukandar, S., Kojima, M.,
674 Sakata, S., 2016. E-waste recycling processes in Indonesia, the Philippines, and
675 Vietnam: A case study of cathode ray tube TVs and monitors. Resources,
676 Conservation and Recycling 106, 48-58.
677
678

679 Supporting Information:

680 **TABLE OF CONTENTS:**

693

694

S1. Adsorption isotherm models

In this study, the Langmuir and Freundlich model were used to describe the adsorption isotherm. The Langmuir model proposes the homogeneity of adsorbent surfaces where each site has equal affinity towards the adsorbate (Foo and Hameed, 2010). This model was derived with the assumption of monolayer adsorption (one molecule thickness) having identical interaction between the adsorbed molecules.

The linearized form of Langmuir equation can be represented by the following equation (Eq. 1):

$$\frac{C_e}{q_e} = \frac{1}{q_{max} K_L} + \frac{C_e}{q_{max}} \quad \text{.....Eq. 1}$$

where, C_e is the equilibrium concentration of remaining metal in the solution (mg L^{-1}), q_e is the amount of a metal adsorbed per unit mass of adsorbent at equilibrium (mg g^{-1}), q_{max} is the amount of adsorbate at complete monolayer coverage (mg g^{-1}), and K_L (L mg^{-1}) is the Langmuir constant.

The Langmuir equation can also be expressed in terms of a dimensionless constant called the separation factor (R_L). The R_L value indicates the favorability of the adsorption process and is calculated according to the following equation (Eq. 2):

$$R_L = \frac{1}{1 + C_m K_L} \quad \text{.....Eq.2}$$

where, C_m is the maximal initial adsorbate concentration (mg L^{-1}). R_L value between 0 and 1 will indicate a favorable adsorption, at $R_L > 1$ the reaction is unfavorable and when $R_L = 0$ it showed irreversible adsorption.

In contrast to Langmuir model, the Freundlich model proposes the formation of multilayer and reversible adsorption. This model emphasizes on the surface heterogeneity together with a non-uniform distribution of adsorption heat and different adsorption affinity of solute

towards the surface sites. The Freundlich model is described by the following equation (Eq. 3):

$$\log q_e = \log K_F + \frac{1}{n}\log C_e \quad \text{.....Eq. 3}$$

where, K_F is denoted as distribution coefficient (L g^{-1}) and n is the empirical constant. The value of n is derived from the slope between log C_e vs log q_e curve while K_F is calculated through the intercept of the Freundlich isotherm plot.

S2. Adsorption kinetic model

Pseudo-first order (Lagergren Model) and pseudo-second order models are expressed as Eq. 4 &5, respectively:

$$\ln (q_e - q_t) = \ln q_e - k_1 t \quad \text{.....Eq. 4}$$

$$\frac{t}{q_t} = \frac{1}{k_2 q_e^2} + \frac{1}{q_e} t \quad \text{.....Eq. 5}$$

where, q_e is the adsorption capacity (mg g^{-1}) at equilibrium, q_t (mg g^{-1}) is the adsorption capacity at time t (min), and k_1 (min^{-1}) and k_2 (g mg^{-1} min^{-1}) is the pseudo-first order and pseudo-second order rate constant, respectively.

Intra-particle diffusion model is described as (Eq.6):

$$q_t = k_i t^{1/2} + C \quad \text{.....Eq. 6}$$

where, q_t (mg g^{-1}) is the adsorption at time t (min), and k_i (mg g^{-1} $min^{0.5}$) is the intra-particle diffusion rate constant while the intercept C represents the boundary layer thickness.

738 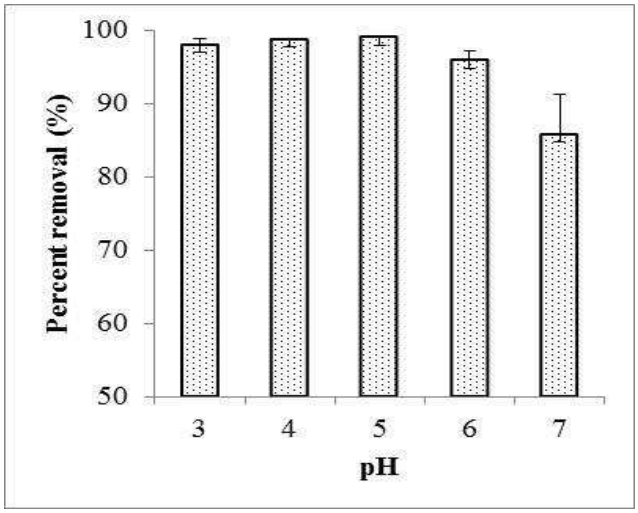

739 SI Fig. 1: Influence of pH on Pb(II) removal by palygorskite-iron oxide nanocomposite (at

740 25°C with 150 agitations min^{-1} and 5 g L^{-1} adsorbent loading)

741

742 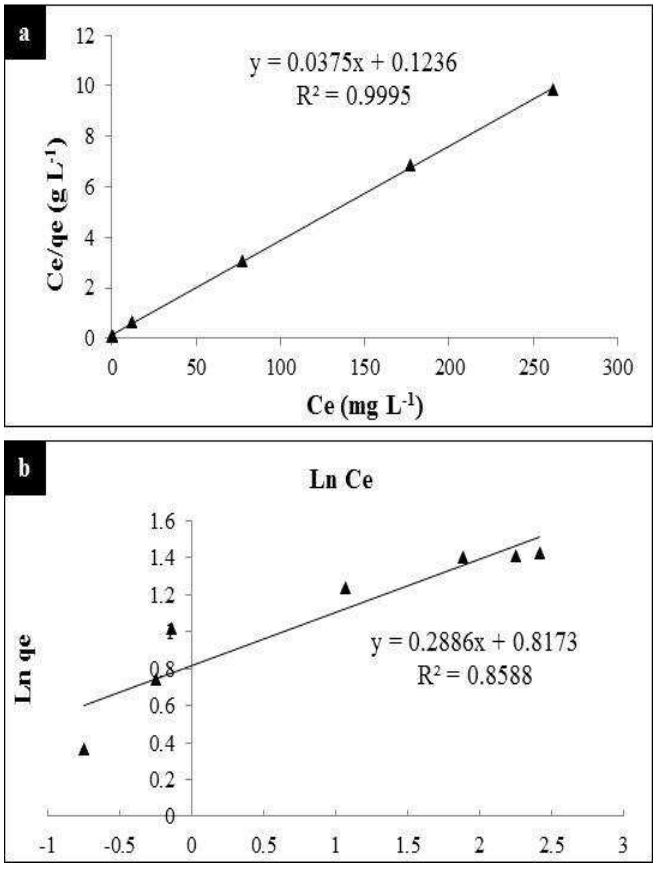

743 SI Fig. 2: Fitting of Pb(II) adsorption data on palygorskite-iron oxide nanocomposite to

744 isothermal models; (a) Langmuir model, and (b) Freundlich model (at 25°C with 150

745 agitations min^{-1}, pH 5 and 5 g L^{-1} adsorbent loading)

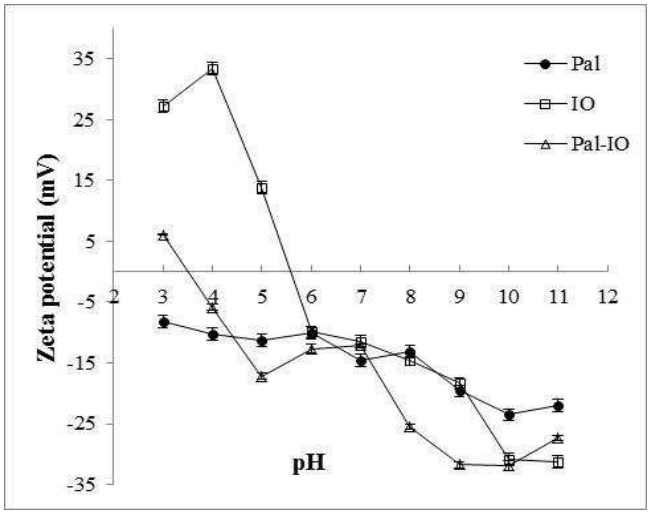

SI Fig.3: Changes in zeta potential values with pH; palygorskite (Pal), iron oxide (IO), and palygorskite-iron oxide nanocomposite (Pal-IO)

SI Table 1: Values of separation factor, R_L, calculated from the Langmuir isotherm constants (K_L) at different initial Pb(II) concentration for palygorskite (Pal), iron oxide (IO), and palygorskite-iron oxide nanocomposite (Pal-IO) at 25°C

Initial concentration (mg L^{-1})	R_L value		
	Pal	IO	Pal-IO
20	0.2693	0.5567	0.1415
50	0.1285	0.3344	0.0618
70	0.0953	0.2641	0.0450
100	0.0686	0.2008	0.0319
200	0.0355	0.1116	0.0162
300	0.0240	0.0773	0.0109
500	0.0145	0.0478	0.0065

Reference

Foo, K.Y., Hameed, B.H., 2010. Insights into the modeling of adsorption isotherm systems. Chemical Engineering Journal 156, 2-10.